American Mineralogist, Volume 110, pages 1171-1185, 2025

Viscosity measurements of selected lunar regolith simulants

Simon Stapperfend[1,*,†], Donald B. Dingwell[2], Kai-Uwe Hess[2,‡], Jennifer Sutherland[3], Axel Müller[4], Dirk Müller[2], Michael Eitel[2], Julian Baasch[1], Stefan Linke[1], and Enrico Stoll[1]

[1]Chair of Space Technology, Technische Universität Berlin, Marchstr. 12-14, 10587 Berlin, Germany
[2]Earth and Environmental Sciences, Ludwig-Maximilians-Universität München, Theresienstraße 41/III, 80333 München, Germany
[3]Institut Laue-Langevin, 71 Av. des Martyrs, 38000 Grenoble, France
[4]OHB System AG, Manfred-Fuchs-Str. 1, 82234 Weßling, Germany

Abstract

In the context of evaluating lunar construction options, this study focuses on characterizing the viscosities and glass transition properties of lunar regolith simulants to support the development of additive manufacturing processes using molten regolith. Employing the modular TUBS lunar regolith simulant system, we measured the viscosities of different simulants through high-temperature experiments conducted between 1051 and 1490 °C using concentric cylinder viscometry in air. Additionally, differential scanning calorimetry (DSC) was utilized to evaluate the glass transition temperatures, which were in the range between 689 and 815 °C. The measured viscosity data were parameterized by the Vogel-Fulcher-Tammann (VFT) equation, which is adept at describing the viscosities and related properties of silicate liquids. The measured viscosities were compared with the predicted values of six viscosity models. The model by Sehlke and Whittington (2016) best predicts the viscosities of the tested lunar regolith simulants at superliquidus temperatures, and no model adequately predicts viscosities at the glass transition temperature, indicating a need for further research in this area. We infer that 3D printing technologies based on molten lunar regolith are, viscosity-wise, best constrained to highland regions. The reduced environment on the Moon influences the 3D printing process in a positive manner.

Keywords: Viscosity, glass transition, fragility, lunar regolith simulant, rheology, differential scanning calorimetry, concentric cylinder, silicate melts, Moon, TUBS-M, TUBS-T

Introduction

The return to the Moon and the associated construction of a permanent and self-sustaining research station on the lunar surface is currently the focus of numerous space agencies and private companies (Crawford 2004; Hufenbach et al. 2014). Due to its near-ubiquitous presence, the lunar regolith offers a potentially limitless supply of raw materials for the production of large surface structures (Johnson and Chua 1993; Wilhelm and Curbach 2014).

The fabrication of components and structures using lunar regolith simulants on Earth has already been demonstrated using, for example, selective laser melting (Gerdes et al. 2018; Reitz et al. 2021; Ginés-Palomares et al. 2023b), microwave sintering (Taylor and Meek 2005; Kim et al. 2021), solar sintering (Meurisse et al. 2018; Fateri et al. 2019b) and D-Shape technology (Cesaretti et al. 2014). Additive manufacturing with molten lunar regolith simulants for the production of structural components is currently being pursued at Technische Universität Berlin (TU Berlin) using a process in which the regolith is electrically melted in a crucible, flows by gravity through a nozzle at the bottom of the crucible, and is then applied in layers to form a solid component after cooling (Stapperfend et al. 2023). As no material additives are foreseen for this process, the material transport effort from Earth can be minimized, reducing costs enormously, especially for large construction projects. The main driving factor for this technology is the melt viscosity (η), which describes a fluid's internal resistance to flow. The viscosity of silicate melts is mainly dependent on the chemical composition, temperature, volatile, and crystal content and has been intensively investigated in the past (e.g., Romano et al. 2003; Lavallée et al. 2007; Giordano et al. 2008; Villeneuve et al. 2008; Di Genova et al. 2013).

Due to the geological diversity of previous landing sites on the Moon and those initially foreseen in the context of the Artemis program, continued characterization of lunar regolith material—particularly under elevated temperature conditions—is required to inform future site selection and the optimization of additive manufacturing technologies. Inherent to high-temperature technologies involving melt manipulation is its flow throughout the printing process. Stresses involved in melt flow will be dictated at superliquidus conditions via the equilibrium Newtonian shear viscosity of the molten regolith.

Against this backdrop of potential large-scale technologies and planetary-scale geological complexity, it may come as a surprise that the high-temperature behavior of lunar regolith and its terrestrial simulants remains largely unexplored. General inferences can be made regarding the potential variation of melt properties from parameterization programs that have been developed following decades of experimental work in the geosciences (Richet 1984; Lange and Carmichael 1987, 1990; Persikov et al. 1990; Dingwell 2006; Neuville 2006; Sehlke et al. 2014). This

* Corresponding author E-mail: s.stapperfend@tu-berlin.de Orcid https://orcid.org/0000-0002-6495-3447

‡ Orcid https://orcid.org/0000-0003-1860-8543

0003-004X/25/0008–1171$05.00/DOI: https://doi.org/10.2138/am-2023-9263

basis, together with the knowledge of the wide chemical range of terrestrial magmatic rocks, as well as of lunar rock and regolith known to us, leads to the expectation that the physical properties of molten regolith will vary widely with both temperature and chemical composition. Although there is some preliminary work on glass production from lunar regolith (Magoffin and Garvey 1990; Mackenzie and Claridge 1979; Schleppi et al. 2019, 2021) and high-temperature behavior of lunar regolith and its simulants (Ray et al. 2010; Street et al. 2010; Morrison et al. 2019; Fateri et al. 2019a; Sehlke and Whittington 2020; Zocca et al. 2020; Farries et al. 2021; Whittington and Parsapoor 2022; Ginés-Palomares et al. 2023a), additional experimental measurements of the high-temperature properties of chemically accurate lunar regolith simulants are necessary to better constrain the role of glass in manufacturing.

In this study, the superliquidus Newtonian shear viscosity of liquids aimed at mimicking returned Apollo compositions was determined, which were generated by the combination of lunar regolith simulants based on the TUBS system developed at the Technische Universität Braunschweig in Germany (Linke et al. 2018, 2020). Viscosities just above the glass transition temperature were determined by applying the "Shift Factor" to the calorimetric results to generate the Vogel-Fulcher-Tammann equation. This contribution is intended as the launch of a campaign to characterize the high-temperature flow behavior of remelted lunar regolith simulants over an adequate range of their likely initial chemistry, mineralogy, and aggregate components, first introduced by Sutherland et al. (2022).

Materials and Methods

Lunar regolith simulants

For this work, simulants from the modular lunar simulant system TUBS were used. The base simulants TUBS-M and TUBS-T correspond to the average chemical composition of the lunar mare and the lunar highland regions, respectively, and were mineralogically and chemically characterized by Linke et al. (2020). An intermediate mixture of the two base simulants, named TUBS-I, was also investigated. Based on the modular simulant system, chemically adapted simulants (CAS) of specific samples from Apollo 17 were created for another research project at TU Berlin (Linke 2022). The CAS were created by mixing the base simulants with raw minerals to chemically mimic specific sampling locations.

The following CAS were generated by Linke (2022) in preparation for a possible lunar technology demonstration of the MOONRISE laser melting payload (Linke et al. 2022):

- Station-5: Mean value from Apollo 17 sample 75061 and 75081
- LRV-6: Apollo 17 sample 74121
- LRV-7/8: Mean value from Apollo 17 sample 75111 (LRV-7) and 75121 (LRV-8)

Concentric cylinder viscometer

The lunar regolith simulant samples prepared at TU Berlin were transported to the Ludwig-Maximilians-Universität München in the form of powders. Approximately 150–200 g of each powder was melted in a thin-walled iron-saturated Pt crucible under direct heating at 1500 °C in a Nabertherm box furnace with Superkanthal $MoSi_2$ heating elements and ZrO_2 fiber inner insulation walls in air. A plate of dense ZrO_2 was laid under the crucible to protect the furnace against any melt spills. The fully melted samples were held at 1500 °C at 1 atm for 2 h. Next, they were removed rapidly from the furnace, and the melt was poured from the thin-walled Pt synthesis crucible directly into a $Pt_{80}Rh_{20}$ viscometry measurement crucible (2.54 cm inner diameter, 5.08 cm inner height, and 1 mm wall thickness), leaving around 5 mm space at the top of the crucible to accommodate the volume of insertion of a viscometry spindle. Two spindles were employed in the present study: a high-viscosity spindle ("Pthv," 3 mm diameter, 43 mm length) and a low-viscosity spindle ("Ptlv," 14.4 mm diameter, 33.2 mm length). The high-viscosity spindle was only used for the TUBS-T simulant, while the low-viscosity spindle was used for all other melts. Both were tapered 45° at the top and bottom to reduce edge effects (Dingwell 1986, 1989; Dingwell and Virgo 1988).

The filled viscometry crucible was transferred directly to a bottom-loading viscometry furnace (Deltech) operating at 1500 °C in air with Superkanthal heating elements and electronic temperature and power management through in-house viscometer and temperature control software. The viscometry crucible sits in a cradle machined from a mullite-based ceramic brick. The viscometry furnace is operated with a Type B ($Pt_{70}Rh_{30}/Pt_{94}Rh_{06}$) thermocouple, which resides within an Al_2O_3 sheath. Sample temperature is calibrated by inserting a Pt-sheathed Type S ($Pt/Pt_{90}Rh_{10}$) measuring thermocouple into the center of the melt in the viscometry crucible, and a temperature correction is obtained. The spindle(s) are suspended from a Brookfield DIII viscometry head (0.7187 mNm full-scale torque), which is controlled and recorded using our software. The samples were stirred for several hours at 1500 °C to remove potential bubbles and to ensure chemical homogeneity. The entire system was calibrated against the soda lime glass viscosity standard DGG-1 of the Deutsche Glastechnische Gesellschaft with an accurately known viscosity-temperature relationship (Meerlender 1974).

The viscometry experiments were initiated at 1500 °C (held for 2 h) and then at successive 25 °C steps of decreasing temperature. This temperature sequence was terminated either by melt crystallization (as indicated by a substantial upward drift of torque at constant temperature) or viscometer instrument limits. By systematic software-driven halving of the viscometer speed upon the obtainment of 100% torque (full-scale reading), a rotation speed over a range of 40 to 0.1 rpm was varied. This, combined with the two spindles available, yields a dynamic range of 6 log units of viscosity determinations from 10°–10^5 Pa s. The dynamic viscosities were calculated by:

$$\log(\eta) = \log(m \cdot M + n)$$

where m and n are parameters depending on the rpm and spindle used, and M is the torque of the spindle. The calibration data of the Ptlv and Pthv spindles are shown in Table 1. All torque values lower than 10% and higher than 90% were omitted from the data set.

Following viscosity determinations, the spindle was retracted vertically from the crucible, quenched, and cleaned with concentrated hydrofluoric acid. The crucible was then removed from the furnace through the bottom door, and the melt

Table 1. Calibration parameters for the rotational viscometer concentric cylinder method

Ptlv (low-viscosity platinum)			Pthv (high-viscosity platinum)		
η = m·M+n			η = m·M+n		
Speed (rpm)	m	n	Speed (rpm)	m	n
40	0.0636	0.3999	40	1.205	−0.7067
20	0.1285	0.2824	20	2.4391	−2.0242
10	0.2569	0.2556	10	4.9607	−5.4643
5	0.5073	0.1167	5	10.242	−19.186
2.5	1.0261	−0.5969	2.5	20.858	−38.912
1.2	2.1444	−3.0637	1.2	44.43	−81.229
0.6	4.3789	−8.2706	0.6	90.176	−166.8
0.3	8.8122	−16.0980	0.3	179.59	−230.97
0.2	13.3390	−25.7250	0.2	295.68	−1157.4
0.1	27.6430	−70.1370	0.1	603.15	−1945.7
0.05	55.9680	−126.9400	0.05	1200.4	−2559.7

was poured from the hot crucible onto a stainless-steel plate for cooling. More viscous melts were left to cool in the viscometry crucible and then drilled from the crucible using diamond corer drills. Comparative measurements of the LRV-6 CAS and LRV-7/8 CAS compositions with similar protocols.

Electron probe microanalysis (EPMA)

The chemical compositions of the glass samples quenched from the viscosity measurements were determined using a Cameca SX-100 electron microprobe at the Department for Earth and Environmental Sciences, LMU Munich. To meet the requirements of the beam-sensitive glass, the following conditions were applied: 15 kV accelerating voltage, 5 nA beam current, and a 10 µm defocused beam. Calibration was performed using the following silicate and oxide standards: albite (Na, Si), orthoclase (K, Al), Fe_2O_3 (Fe), periclase (Mg), wollastonite (Ca), rutile (Ti), bustamite (Mn), Cr_2O_3 (Cr), apatite (P). Only results with totals between 98.5–101.5 wt% were accepted for evaluation. The relative error of the measurements is <2%.

Magnetization measurements

To detect and quantify possible magnetic crystals that formed during the quenching of melts, magnetic hysteresis has been measured on a 3900 MicroMag Vibrating Sample Magnetometer at the LMU München. This is performed by exposing a sample to an external magnetic field. Simultaneously, pickup coils measure the magnetic moment of the vibrating sample as a function of the external field and the magnetization history, which is called hysteresis loop.

Differential scanning calorimetry

The quenched glasses were investigated using differential scanning calorimetry (Netzsch DSC 404 C/3/F1 Pegasus) to determine their glass transition temperatures (T_g). The calorimeter was calibrated for temperature and sensitivity using the melting temperature of indium and gold to within ±2 °C. For the measurement of the glass transition temperature, ~20 mg of the post-viscometry glass was transferred to a Pt crucible and then analyzed under a dynamic argon (20 cm^3/min) atmosphere. To structurally relax the glasses, the samples were heated at 10 °C/min to about 50 °C above the peak of the glass transition temperature. The samples were then cooled to room temperature at 10 °C/min and again heated at 10 °C/min to obtain T_g defined as the peak temperature. A cooling and heating rate of 10 K/min is sufficient to produce a homogeneous and practically crystal-free glass. Comparative measurements of the LRV-6 CAS and LRV-7/8 CAS compositions were performed with similar protocols.

Results

Chemical composition of remelted simulants

Table 2 displays the chemical compositions of all simulants. The SO_3 and Cl concentrations in all samples are below the detection threshold of 0.13 and 0.06 wt%, respectively, and are therefore not mentioned. Notably, the measured Fe_2O_3 (Total) and TiO_2 concentrations in the CAS samples differ from those reported by (Linke 2022). As the redox state was not measured in this work, the iron oxidation state was calculated using the model by Kress and Carmichael (1991). The melt's structure can be quantified using parameters such as the number of non-bridging oxygen atoms per tetrahedron (NBO/T) (Mysen 1988) and the structure modifier content (SM) (Giordano and Dingwell 2003). NBO/T indicates the degree of polymerization within the melt, where higher values suggest less-polymerized structures. SM represents the sum of network modifier oxides in mol%: $SM = x_{FeO} + x_{MgO} + x_{MnO} + x_{CaO} + x_{Na_2O} + x_{K_2O}$ (Giordano and Dingwell 2003). In the superliquidus range, the absolute viscosity increases with decreasing NBO/T. The calculated NBO/T and SM of the measured samples are displayed in Table 4. For all compositions, f_{O_2} was adjusted to a fixed value of 0.21 (air), corresponding to atmospheric conditions.

Table 2. Chemical compositions measured by electron microprobe analysis of lunar simulants after viscometry measurements and original data by Linke (2022)

	TUBS-M		TUBS-T		TUBS-I		Station-5 CAS		LRV-6 CAS		LRV-7/8 CAS		
	This work[b]	(Linke 2022)	This work[b]	(Linke 2022)	This work[b]	(Linke 2022)	This work[b]	(Linke 2022)	This work[b]	(Linke 2022)	This work[b]	(Linke 2022)	[b]Det. Lim.
SiO_2	49.07	48.61	48.92	48.71	49.04	48.66	42.75	41.88	45.65	45.34	46.55	46.04	0.15
TiO_2	2.47	2.29	0.17	0.12	1.38	1.205	10.62	8.18	5.43	4.12	5.58	4.33	0.13
Al_2O_3	13.55	13.29	30.16	30.33	21.66	21.805	13.14	12.92	20.26	20.20	15.18	15.12	0.13
Fe_2O_3(T)	10.93		1.46		6.44		12.65		7.70		10.83		0.22
FeO(T)		10.14		1.05		5.595		15.08		8.41		11.06	
Na_2O	3.97	3.67	3.09	3.05	3.44	3.36	3.11	3.07	3.13	3.049	3.41	3.38	0.13
K_2O	1.82	1.71	0.29	0.22	1.02	0.965	1.36	1.32	0.89	0.85	1.47	1.40	0.08
MgO	8.28	8.73	0.89	0.57	4.70	4.65	7.30	7.17	5.28	5.14	6.97	7.06	0.09
CaO	8.25	8.31	13.91	14.57	11.22	11.44	7.76	7.61	10.37	10.52	8.75	8.78	0.11
MnO	0.17	0.18	<d.l.	0.02	0.10	0.10	0.28	0.19	0.17	0.11	0.21	0.16	0.06
Cr_2O_3	<d.l.	0.04	<d.l.	0.00	<d.l.	0.02	0.17	0.03	0.10	0.02	0.09	0.03	0.07
P_2O_5	0.53	0.51	0.04	0.00	0.28	0.255	0.42	0.39	0.26	0.22	0.43	0.41	0.04
Total	**99.04**	**97.48**	**98.93**	**98.64**	**99.27**	**98.055**	**99.56**	**97.84**	**99.22**	**97.979**	**99.48**	**97.77**	
Fe_2O_3[a]	7.39		0.91		3.98		7.51		4.67		6.57		
FeO[a]	4.30		0.51		2.27		4.76		2.81		3.93		
Fe^{3+}/Fe_{tot}[a] (molar%)	0.61		0.62		0.61		0.59		0.60		0.60		
Fe^{2+}/Fe_{tot}[a] (molar%)	0.39		0.38		0.39		0.41		0.40		0.40		

Notes: The relative error for the electron microprobe analysis is <2%. All values given in wt%.
[a] Calculated using the method by Kress and Carmichael (1991).
[b] Detection limit (Det. Lim. applies for only the data of this work).

Table 3. High-temperature viscosity data

		$\log_{10}$ η (Pa s)					
T real (°C)	10 000/*T* (K^{-1})	TUBS-M	TUBS-T	TUBS-I	Station-5 CAS	LRV-6 CAS	LRV-7/8 CAS
1490	5.67	0.38	1.17	0.77	0.09	0.45	0.30
1465	5.75	0.45	1.30	0.86	0.14	0.53	0.36
1441	5.83	0.52	1.44	0.96	0.20	0.62	0.44
1417	5.92	0.60	1.58	1.07	0.26	0.71	0.51
1392	6.00	0.69	1.73	1.18	0.32		0.60
1368	6.09	0.78	1.88	1.29	0.39	0.90	0.69
1344	6.18	0.88		1.41	0.47	1.01	0.78
1319	6.28	0.98	2.20	1.54		1.13	0.88
1295	6.38					1.26	0.99
1271	6.48	1.21	2.57	1.82			
1246	6.58	1.33	2.77			1.52	
1222	6.69	1.46		2.13			
1198	6.80	1.60	3.21				
1173	6.91		3.46	2.50			
1149	7.03		3.72	2.70			
1125	7.15		4.00				
1100	7.28		4.32	3.15			
1076	7.41		4.66				
1051	7.55			3.66			

Note: The error is ±log 0.02 Pa s.

High-temperature viscosity

The high-temperature viscosities measured in air are presented in Table 3. All simulants investigated showed the characteristic decreasing viscosity of silicate melts with increasing temperature. The highland simulant TUBS-T has the highest viscosity values throughout the whole temperature range, which is expected to be due to the largest amount of network formers of all tested melts and results in low NBO/T and SM values.

Glass homogeneity

Glass homogeneity was assessed using an electron probe microanalyzer (EPMA) with a backscattered electron (BSE) detector. This analysis revealed subtle heterogeneity in the form of possible phase separation in the post-viscometry samples of the Station-5 simulant. Due to the limited scope of this study, further exploration of this heterogeneity was not feasible. Consequently, only the high-temperature viscosity measurements for the Station-5 simulant were used, and differential scanning calorimetry (DSC) data of this sample were excluded from further investigation.

The homogeneity of the glasses was also assessed by rock magnetic analysis. Figure 1 shows the weight-normalized hysteresis loops of 6 samples after adjustment for dia-/paramagnetic contributions. An original hysteresis loop of a sample that contains only dia-/paramagnetic, and no ferromagnetic particles would look like a straight line with a specific slope. If ferromagnetic particles are present in the sample, their contribution will overlay the line in a limited field range until saturation is reached, and magnetization will develop linearly with the external field. By subtracting the linear slope of the high-field part of the original hysteresis loop from the complete curve, the corrected hysteresis loop, which only shows the ferromagnetic fraction, can be obtained. As an example, for sample LRV-7/8, in addition to the corrected hysteresis loop, the paramagnetic part is also shown, as well as the original curve that represents the sum of the para- and ferromagnetic curves.

Samples TUBS-M, TUBS-T, and TUBS-I exhibit no magnetic remanence. Their original hysteresis loops resemble more or less two straight lines with positive slopes and no opening indicative of paramagnetic magnetic contributors. The shape of the corrected hysteresis loop, covering mainly the upper left and the lower right quadrant, is not a real physical result and excludes the presence of an amount of ferromagnetic crystals like (titano)magnetite or -hematite exceeding our detection limit, which we estimate below the order of 0.01 wt%.

Samples Station-5, LRV-6, and LRV-7/8 also show closed hysteresis loops; in the case of Station-5 curvature is not seen, indicating the absence of a significant amount of (titano)magnetite or -hematite. The hysteresis loops of LRV-6 and LRV-7/8 are also closed but curved. Therefore, it is assumed that these samples contain (titano)magnetite of a superparamagnetic grain size [< ~30 nm; e.g., (Dunlop 1973; Dunlop and Özdemir 1997)]. LRV-6 and LRV-7/8 reach a saturation magnetization of 27.5 and 319.7 mAm^2/kg, respectively. Using the value of 96 mAm^2/kg for pure magnetite, this translates into a weight percentage of (titano)magnetite of 0.0287 and 0.333%, respectively, which can be considered insignificant.

Glass transition temperature

The DSC measurements near the glass transition temperature are shown in Figure 2. The calorimetric glass transition temperature ($T_{g,DSC}$) depends on the cooling rate of the samples in the DSC and, therefore, does not necessarily correspond to the viscometric glass transition temperature (here denoted as $T_{g,12}$), defined as the temperature where the viscosity of the sample is at 10^{12} Pa s (e.g., Richet 1984; Dingwell and Webb 1989; Webb and Dingwell 1990). The viscosity at the calorimetric glass transition temperature can be calculated by using the so-called "Shift Factor," which is dependent on the composition of the samples (Gottsmann et al. 2002). The "Shift Factor" has been determined by using the mol% of excess oxides (*x*), which is a compositional parameter calculated by summation of molar percentages of network modifying oxides (FeO, MnO, MgO, CaO, Na_2O, K_2O, P_2O_5, H_2O), from which the molar

Table 4. Chemical and VFT parameters of discussed compositions after viscosity measurement

	NBO/T[a]	SM[b](mol%)	A_{VFT} (Pa s)	Standard error[c]	B_{VFT}(K)	Standard error[c]	C_{VFT}(K)	Standard error[c]	$T_{g,12}$[c](K)	$T_{g,DSC}$[d](K) (error: ±2 K)	Excess oxides(mol%)	K[e](Pa K) (error: ±0.1 Pa K)	log η at $T_{g,DSC}$ (Pa s) (error: ±0.1 log Pa s)	m_{12}[f]
TUBS-M	0.53	32.22	−2.82	0.02	3349	27	711	1.6	937	962	20.20	9.79	10.57	61
TUBS-T	0.05	22.77	−3.97	0.02	5307	28	732	1.4	1064	1088	2.20	10.20	10.9	51
TUBS-I	0.26	27.47	−3.80	0.06	5150	73	631	3.8	957	987	11.68	9.89	10.67	46
Station-5 CAS	0.47	30.16									18.88			
LRV-6 CAS	0.30	28.00	−2.96	0.02	3458	27	782	1.6	977	1001	12.86	9.87	10.65	63
LRV-7/8 CAS	0.44	30.20	−2.53	0.02	2765	21	711	1.3	972	993	17.91	9.81	10.60	74

[a] Non-bridging oxygen per tetrahedra on a molar basis (Mysen 1988).
[b] Sum of structure modifier oxides (normalized mol%): $SM = x_{FeO} + x_{MgO} + x_{MnO} + x_{CaO} + x_{Na_2O} + x_{K_2O}$ according to Giordano and Dingwell (2003).
[c] Viscometric glass transition temperature (here denoted as $T_{g,12}$) at a viscosity of 10^{12} Pa s derived from VFT-fit parameters.
[d] Corrected calorimetric glass transition temperature (peak).
[e] "Shift Factor" according to Gottsmann et al. (2002).
[f] Fragility index with $T_{g,12}$ at 10^{12} Pa s. Calculated by $m_{12} = B_{VFT}/[T_{g,12}(1 - \{C_{VFT}/T_{g,12}\}^2)]$.

percentages of network forming oxides (Al_2O_3, TiO_2, and Fe_2O_3) are subtracted (Gottsmann et al. 2002). The excess oxides were calculated using the iron oxidation state derived using the model by Kress and Carmichael (1991).

The viscosity at the calorimetric glass transition temperature can then be calculated by applying the relationship:

$$\log_{10}\eta(\text{at } T_{g,DSC}) = K - \log_{10}|q|$$

where η is the dynamic viscosity at the glass transition (here $T_{g,DSC}$) in Pa s, K the calculated "Shift Factor," and q the cooling rate in °C/s (here: 0.17 °C/s). The "Shift Factor" can be calculated by:

$$K = 10.321 - 0.175 \ln(x)$$

where x is the mol% of excess oxides. Note that K in Gottsmann et al. (2002) is defined at the peak of the glass transition temperature.

The low-viscosity data (at superliquidus temperatures) can then be combined with these additional high-viscosity data to allow for a VFT-fit. The measured glass transition temperatures and derived viscosity values are reported in Table 4. During the heating and cooling cycle of the DSC, no exothermic (crystallization) peaks were detected, meaning that there is no change in the homogeneity created by these measurements.

Viscosity-temperature relationship

By grouping the viscosity at the calorimetric glass transition temperature with the experimental high-temperature viscosity data, the non-Arrhenian temperature-dependent viscosity can be approximated with the Vogel-Fulcher-Tammann (VFT) equation (Vogel 1921; Fulcher 1925; Tammann and Hesse 1926):

$$\log_{10}\eta = A_{VFT} + \frac{B_{VFT}}{T - C_{VFT}}$$

where the relationship between viscosity (η in Pa s) and temperature (T in K) depends on parameters A_{VFT} (pre-exponential term), B_{VFT}, and C_{VFT} (Vogel temperature, sometimes denoted as T_0) modeled from viscosity measurements in a wide range of geochemical compositions (Giordano et al. 2008). The VFT parameters were obtained by fitting the high-temperature viscosity data and the DSC-derived viscosity data at $T_{g,DSC}$ (peak) by the method of Gottsmann et al. (2002) to the Vogel-Fulcher-Tammann equation using nonlinear regression, ensuring an optimal representation of the temperature-dependent behavior of the viscosity.

The measured high-temperature viscosity values, the viscosity at the glass transition temperature, and the fitted viscosity curve are displayed in Figure 3. The corresponding VFT-parameters are shown in Table 4.

Discussion

Fragility

The concept of fragility, first introduced by Angell (1991), plays a pivotal role in understanding the departure of a liquid's viscosity from an Arrhenian temperature dependence. This property is a measure of the departure from Arrhenian

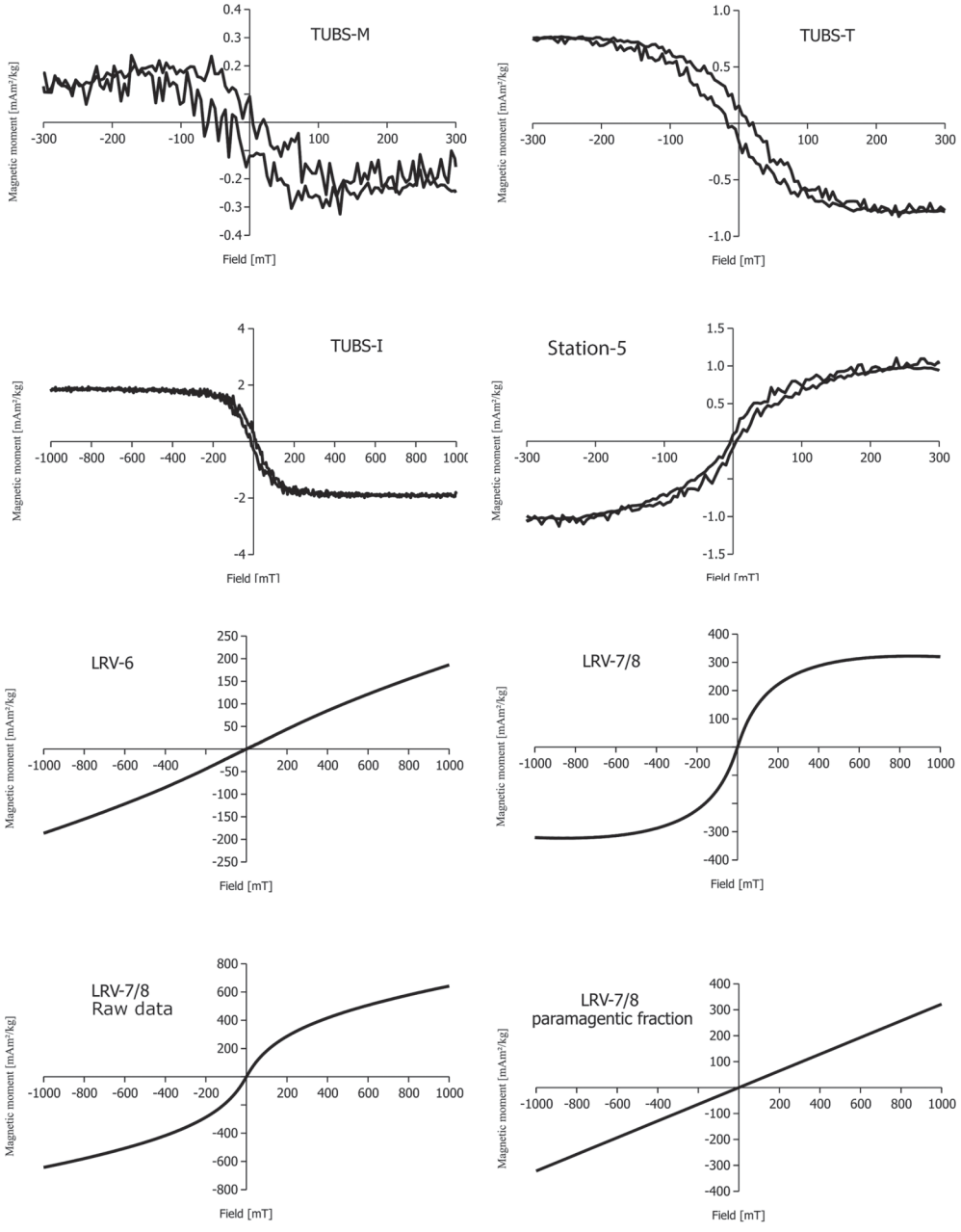

FIGURE 1. Weight normalized corrected hysteresis loops of the quenched simulant samples (top six graphs) as well as raw data and paramagnetic fraction data of the LRV-7/8 sample (bottom two graphs).

temperature dependence of viscosity. Fragility has been defined as the slope of the logarithmic viscosity curve at the viscometric glass transition temperature (here denoted as $T_{g,12}$), when plotted on a reduced temperature scale. The fragility index (m) can be calculated according to (Plazek and Ngai 1991; Böhmer and Angell 1992):

$$m = \left.\frac{d\log_{10}\eta}{d(T_{g,12}/T)}\right|_{T=T_{12}}$$

This parameter has been widely employed to differentiate various types of melts and has proven indispensable in this regard (Hess et al. 1996; Toplis et al. 1997; Avramov 2011; Dingwell et al. 2022). Glassmakers have used fragility as a concept that helps to evaluate the time they have to shape the glass within the working range, which is typically between 10^3–$10^{6.6}$ Pa s (Le Bourhis 2007; Zheng and Mauro 2017).

The degree of fragility within a melt is mostly influenced by its composition. As the degree of polymerization decreases, the fragility tends to increase (Hess et al. 1995; Giordano and Dingwell 2003; Giordano et al. 2009; Russell et al. 2022). Consequently, more fragile liquids exhibit heightened variations in viscosity with temperature changes, demonstrating low viscosity at high temperatures and high viscosity at low temperatures. On the other hand, stronger liquids exhibit higher viscosities at elevated temperatures than fragile liquids. These characteristics jointly serve to inhibit the nucleation

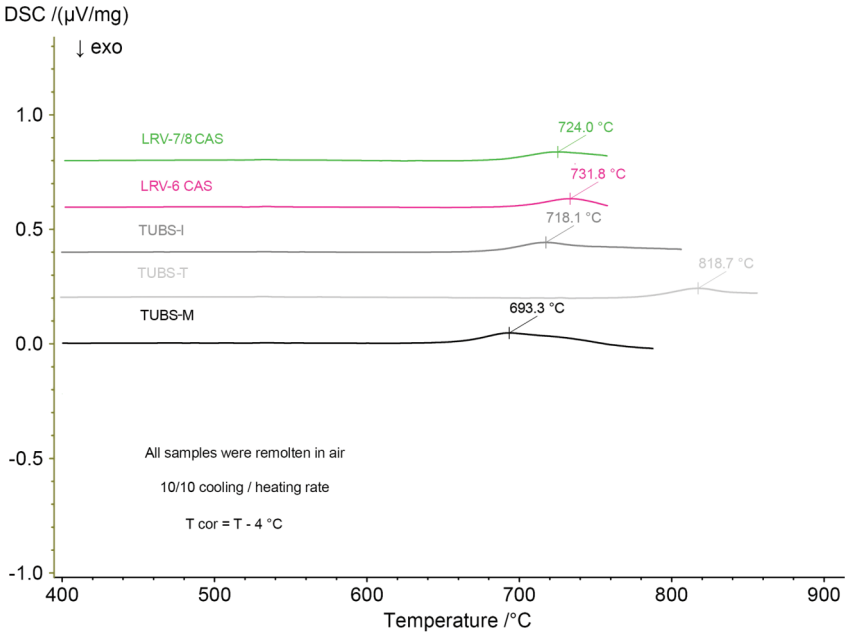

Figure 2. DSC measurements near the glass transition temperature of the tested lunar regolith simulants. Presented data are stacked for visualization with an offset of 0.2 µV/mg. Data of TUBS-M not shifted.

and growth of crystal phases, thereby facilitating the process of glass formation of less-fragile melts (Kelton 2017). The fragility of the melts was calculated and is shown in Figure 4 with an Angell plot. All analyzed samples have high fragilities, ranging from 35 for the TUBS-I simulant up to 59 for the LRV-7/8 CAS.

Comparison with viscosity models

The measured viscosities of the regolith simulants were compared with the well-established viscosity models of Shaw (1972), Giordano et al. (2008) (hereafter GRD), Sehlke and Whittington (2016), and Duan (2014), as well as more recent models based on artificial neural networks: ViscCalc (Langhammer et al. 2022) and GlassNet (Cassar 2023).

The models were implemented as follows:

Shaw (Shaw 1972): The Shaw model predicts Arrhenian behavior, is based on Bottinga and Weill (1972) and is fitted on 2440 data points and compositions ranging from "lunar basalt" to "terrestrial rhyolites" and "hydrous granites of ternary minimum composition." According to the original reference of the model, MnO and P_2O_5 were excluded. Al_2O_3 and Fe_2O_3 are converted

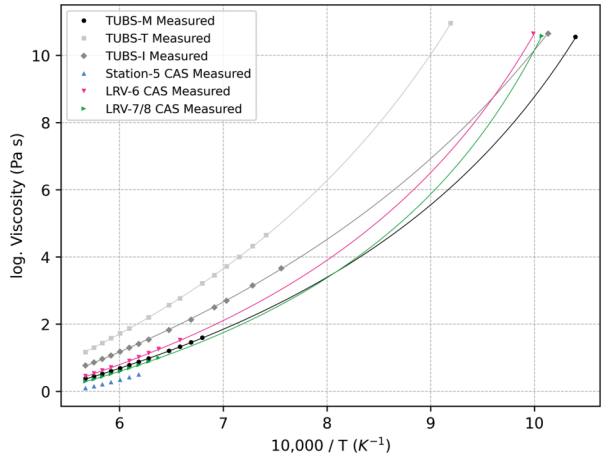

Figure 3. Viscosity data of measured lunar regolith simulants. High-temperature viscosity data measured with concentric cylinder viscometer, low-temperature viscosity data derived from differential scanning calorimetry measurements. Solid line is the corresponding Vogel-Fulcher-Tammann equation.

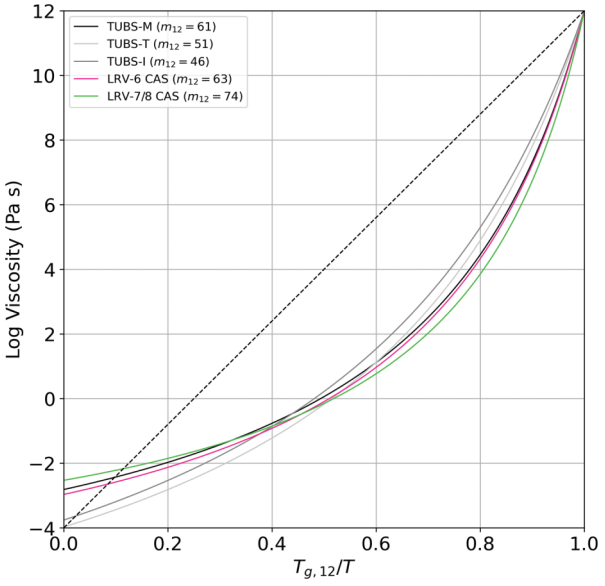

Figure 4. Angell plot of the log viscosity as a function of the scaled inverse temperature. $T_{g,12}$ is the temperature at which the shear viscosity reached 10^{12} Pa s. The dashed line represents a strong liquid with ideal Arrhenian behavior.

to FeO and AlO_2, respectively, by doubling the moles of Fe_2O_3 and Al_2O_3 as was done by Bottinga and Weill (1972). Total oxides (excluding MnO and P_2O_5) were normalized to 1 on a molar basis and used for further calculation of the mean slope, which represents the average contribution of each oxide's slope to the overall viscosity-temperature relationship. The dynamic viscosity can then be calculated (in Poise) by applying the formula:

$$\ln \eta = s \cdot \frac{10^4}{T} - 1.5 \cdot s - 6.4$$

where s is the characteristic slope for a given melt composition.

GRD (Giordano et al. 2008): The GRD model predicts VFT parameters and thus acknowledges the non-Arrhenian behavior of melts. It is fitted on 1774 experimental viscosity data points from 178 different melts ranging in composition from basanite through phonolite and trachyte, to dacite. All Fe_2O_3 in this model is converted to FeO, resulting in:

$$FeO(T) = Fe_2O_3(T) \cdot 0.9$$

Total oxides were normalized to 1 on a molar basis and used for further calculation of the VFT parameters.

Duan (Duan 2014): The model by Duan incorporates pressure and the redox state for natural iron-bearing melts (from ultramafic, mafic to silicic). It is calibrated on ~200 experiments, measurements performed on 19 basaltic melt compositions, and relies on the VFT equation with a fixed "A" value of –4.753468 to capture the non-Arrhenian temperature-dependent viscosity behavior. To evaluate the model, a pressure of 1 bar was used. In cases where the iron oxidation state is not given, Duan used the method of Moretti (2005) to calculate the redox state as a function of oxygen fugacity, pressure, temperature, melt composition, and H_2O content. In this work, the redox state was calculated using the model by Kress and Carmichael (1991).

Sehlke and Whittington (Sehlke and Whittington 2016): This model was developed to predict the viscosity of planetary melts and is fitted on 496 experimental data points from 20 anhydrous tholeiitic planetary basaltic melt compositions at 1 atm. Fifteen of these compositions represent known or estimated surface compositions of Mars, Mercury, the Moon, Io, and Vesta. The model performed well for previous lunar viscosity data and outperformed the GRD model for the tested planetary compositions. As this model was designed for a wide range of oxygen fugacities, the calculated redox state using the model Kress and Carmichael (1991) was used.

ViscCalc (Langhammer et al. 2022): The ViscCalc model was trained on 1603 data points of 50 anhydrous volcanic melts. It is based on the physically motivated MYEGA model (Mauro et al. 2009):

$$\log_{10}\eta(T) = \log_{10}\eta_\infty + \frac{T_g}{T}(12 - \log_{10}\eta_\infty) \cdot \exp\left[\left(\frac{T_g}{T} - 1\right)\left(\frac{m}{12 - \log_{10}\eta_\infty} - 1\right)\right]$$

where $\log_{10}\eta_\infty$ is the asymptotic viscosity at infinitely high temperature, m the fragility index, and T_g the glass transition temperature, which is defined at 10^{12} Pa s for the MYEGA equation. Langhammer used the notation $A = \log_{10}\eta_\infty$ with a fixed value of –2.9. As the model differentiates between the redox state of iron, the values are calculated by using the Kress and Carmichael (1991) model.

GlassNet (Cassar 2023): This model is trained on more than 795 000 data points over 218 000 different glass compositions, implemented using the SciGlass database. Predictions are based on the MYEGA equation, considering the fragility index m, the glass transition temperature T_g, and the asymptotic viscosity A. To properly apply this model, the Kress and Carmichael (1991) redox state of iron was used.

The characteristic parameters needed to calculate the viscosity using the six tested viscosity models are shown in Table 5. To assess which model is most appropriate for modeling the viscosity of the lunar regolith simulants, the root mean square error (RMSE) was employed:

$$\mathrm{RMSE} = \sqrt{\frac{\sum_{n=1}^{N}(\eta_{c,n} - \eta_{m,n})^2}{N}}$$

To obtain comparable values, only the seven highest-temperature viscosity points in the temperature range between 1344 and 1490 °C were considered in the RMSE calculation. The accuracy of the models at the glass transition temperature was compared by calculating the difference between the predicted viscosity at the measured glass transition temperature and the measured glass transition viscosity. The comparison of the viscosity measurements with the predictions based on the six models is shown in Figure 5 and Table 6. The comparison of only the high-temperature viscosity is displayed in Figure 6.

The Shaw model provides good high-temperature viscosity predictions, with an RMSE (superliquidus) ranging from 0.126 to 0.261 log units (Mean RMSE: 0.186 log units). However, it exhibits a significant deviation at the glass transition, with a difference of 5.26 to 6.26 log units [Mean $\Delta\eta(T_g)$: 5.86 log units], attributed to its underlying Arrhenian basis.

The GRD model yields moderate accuracy with an RMSE (superliquidus) spanning 0.071 to 0.893 log units [Mean RMSE: 0.451 log units] and a glass transition difference between 0.13 and 2.63 log units [Mean $\Delta\eta(T_g)$: 1.07 log units].

Duan's model proves to be the least efficient for the given compositions, showing an RMSE between 0.637 and 1.784 log units (Mean RMSE: 1.316 log units). The glass transition temperature is predicted with a difference of 0.79 to 2.02 log units [Mean $\Delta\eta(T_g)$: 1.34 log units].

Sehlke and Whittington's model performed the best, with a quite consistent RMSE in the high-temperature regime, ranging from 0.020 to 0.078 log units (Mean RMSE: 0.052 log units). However, it falls off in predicting the glass transition temperature, with a difference of 0.41 to 1.98 log units [Mean $\Delta\eta(T_g)$: 0.97 log units].

Langhammer's ViscCalc, an artificial neural network model, presents a moderate RMSE (superliquidus) between 0.057 and 0.397 log units (Mean RMSE: 0.243 log units). The difference in the glass transition temperature varies from 0.03 to 0.97 log units [Mean $\Delta\eta(T_g)$: 0.37 log units], making it the best model for predicting the glass transition temperature.

The GlassNet model, the most recent and based on artificial neural networks, exhibits an RMSE in the high-temperature

Table 5. Resulting parameters from the different viscosity models

	TUBS-M	TUBS-T	TUBS-I	Station-5 CAS	LRV-6 CAS	LRV-7/8 CAS
s[a]	2.19	2.68	2.45	1.98	2.26	2.18
A_{VFT} (Pa s)[b]	−4.55	−4.55	−4.55	−4.55	−4.55	−4.55
B_{VFT} (K)[b]	5719	5361	5568	5781	5513	5722
C_{VFT} (K)[b]	587	672	630	677	670	633
T_g (K)[c]	945	1034	950	977	966	960
m[c]	48	43	38	49	43	51
A (log Pa s)[d]	−3.00	−3.20	−2.97	−2.51	−2.90	−2.72
T_g (K)[d]	928	1048	994	935	983	949
m[d]	41	43	43	43	42	42
A_e (log Pa s)[e]	−3.34	−3.34	−3.34	−3.34	−3.34	−3.34
B_e (J mol^{-1}) [e]	161 184	189 124	176 190	159 231	171 182	163 739
S^{conf} (mol^{-1} K^{-1})[e]	10.87	13.47	12.39	11.02	12.19	11.32
C^{p}_{conf} (J mol^{-1} K^{-1})[e]	22.8	19.7	21.3	24.2	22.5	22.9
T_g^{3R*} (K)[e]	927	1,053	987	900	958	932
A_{VFT} (Pa s)[f]	−4.75	−4.75	−4.75	−4.75	−4.75	−4.75
B_{VFT} (K)[f]	8162	8264	8209	8163	8194	8175
C_{VFT} (K)[f]	491	504	497	491	495	492

[a] According to Shaw (1972).
[b] According to Giordano et al. (2008).
[c] According to Langhammer et al. (2022).
[d] According to Cassar (2023).
[e] According to Sehlke and Whittington (2016).
[f] According to Duan (2014).

regime ranging from 0.066 to 0.541 log units (Mean RMSE: 0.292 log units). It excels at the glass transition, displaying a viscosity difference between 0.06 and 1.66 log units [Mean $\Delta\eta(T_g)$: 0.63 log units].

Consequently, the model by Sehlke and Whittington (2016), which was calibrated specifically for planetary melts, also emerges as the most suitable choice for the accurate prediction of superliquidus viscosities within the tested melt compositions. It excels in providing precise estimates of high-temperature viscosities. The model by Langhammer et al. (2022) performed best at predicting the DSC-derived viscosity values at the glass transition temperature. However, it is imperative to underscore that none of the models demonstrate the requisite accuracy in anticipating viscosities at the glass transition temperature for all the tested samples. This limitation highlights the ongoing challenge of adequately modeling glass transition phenomena, signaling the need for further investigation and model refinement in this domain.

Expected results on the Moon

Previously it has been shown that the oxidation state and structure of iron play a decisive role in the structure and properties of silicate melts (e.g., Mysen et al. 1984; Chevrel et al. 2013, 2014; Cukierman and Uhlmann 1974; Dingwell 1988, 1991; Dingwell and Virgo 1987, 1988; Giuli et al. 2011; Knipping et al. 2015; Lange and Carmichael 1987; Toplis and Carroll 1995; Toplis et al. 1994).

The Fe_2O_3-FeO ratio of silicate melts depends on temperature, chemical composition, and redox state, which is expected to be very low on the Moon (e.g., Richet and Bottinga 1986; Kress and Carmichael 1991; Jackson et al. 1993; Wilke et al. 2001, 2006; Giuli et al. 2003; Magnien et al. 2008). As shown by Cukierman and Uhlmann (1974), heavily reduced melts, like those expected on the Moon, have a lower glass transition temperature than melts created using terrestrial materials but have a similar form of the variation of viscosity with temperature near the glass transition.

The influence of the oxidation state of highly reduced lunar regolith simulants should be investigated in more detail in further measurement campaigns to validate the applicability of the Earth-based viscosity models to actual lunar regolith. Real lunar regolith, in contrast to all existing lunar regolith simulants, is characterized by a significant reduction in oxygen content, critically impacting melt viscosity. Iron in this regolith is primarily found as ferrous iron (Fe^{2+}), with a smaller fraction existing as metallic iron (Fe^0) (e.g., Wieczorek 2006; Lucey et al. 2018). Iron oxides, specifically FeO and Fe_2O_3, serve as key influencers of melt viscosity, acting as network modifiers and network formers within the silicate melt structure (Liebske et al. 2003; Bouhifd et al. 2004; Stabile et al. 2016; Di Genova et al. 2017). FeO, functioning as a network modifier, disrupts the silicate network by breaking Si-O bonds, leading to a reduction in viscosity. Conversely, Fe_2O_3, acting as a network former, enhances the structured silicate network by contributing bridging oxygen atoms, consequently elevating melt viscosity. Experiments on synthetic silicate liquids at a fixed temperature at superliquidus and different oxygen fugacities performed by Chevrel et al. (2014) showed that the viscosity of more-reduced samples slightly decreases until $Fe^{2+}/Fe_{tot} = 0.6$ and increases slightly after a ratio of $Fe^{2+}/Fe_{tot} > 0.6$ is reached.

It was further shown that the glass transition temperature increases with a decreasing Fe^{2+}/Fe_{tot} ratio (Liebske et al. 2003; Bouhifd et al. 2004; Di Genova et al. 2017). Research on lunar iron-rich basalts by Cukierman and Uhlmann (1974) found that changing the Fe^{2+}/Fe_{tot} ratio from 0.94 to 0.76 had no impact on the viscosity near the glass transition. However, adjusting the

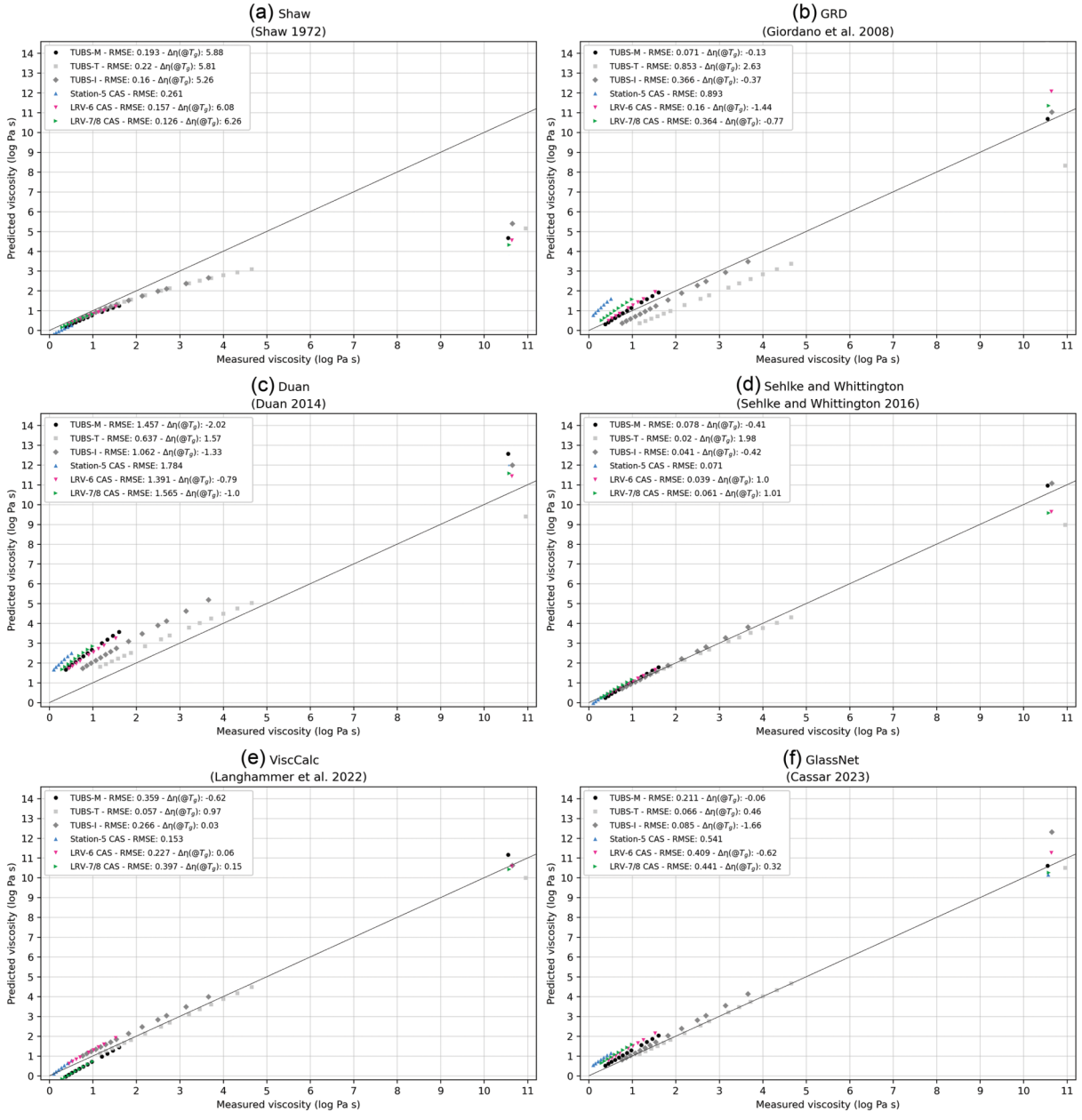

Figure 5. Comparison of measured viscosity and DSC-derived viscosity data against predicted viscosities. All values given in log units.

Table 6. Performance of the viscosity models

	Shaw		GRD		Duan		Sehlke and Whittington		Langhammer (ViscCalc)		Cassar (GlassNet)	
	RMSE	$\Delta\eta(T_g)$	RMSE	$\Delta\eta(T_g)$	RMSE	$\Delta\eta(T_g)$	RMSE	$\Delta\eta(T_g)$	RMSE	$\Delta\eta(T_g)$	RMSE	$\Delta\eta(T_g)$
TUBS-M	0.193	5.88	0.071	−0.13	1.457	−2.02	0.078	−0.41	0.359	−0.62	0.211	−0.06
TUBS-T	0.220	5.81	0.853	2.63	0.637	1.57	0.020	1.98	0.057	0.97	0.066	0.46
TUBS-I	0.160	5.26	0.366	−0.37	1.062	−1.33	0.041	−0.42	0.266	0.03	0.085	−1.66
Station-5 CAS	0.261		0.893		1.784		0.071		0.153		0.541	
LRV-6 CAS	0.157	6.08	0.160	−1.44	1.391	−0.79	0.039	1.00	0.227	0.06	0.409	−0.62
LRV-7/8 CAS	0.126	6.26	0.364	−0.77	1.565	−1.00	0.061	1.01	0.397	0.15	0.441	0.32
Mean	0.186	5.86	0.451	1.07	1.316	1.34	0.052	0.97	0.243	0.36	0.292	0.63

Notes: Only the seven highest temperature viscosity data points in the temperature range between 1344 and 1490 °C were considered in the RMSE calculation. All values given in log units.

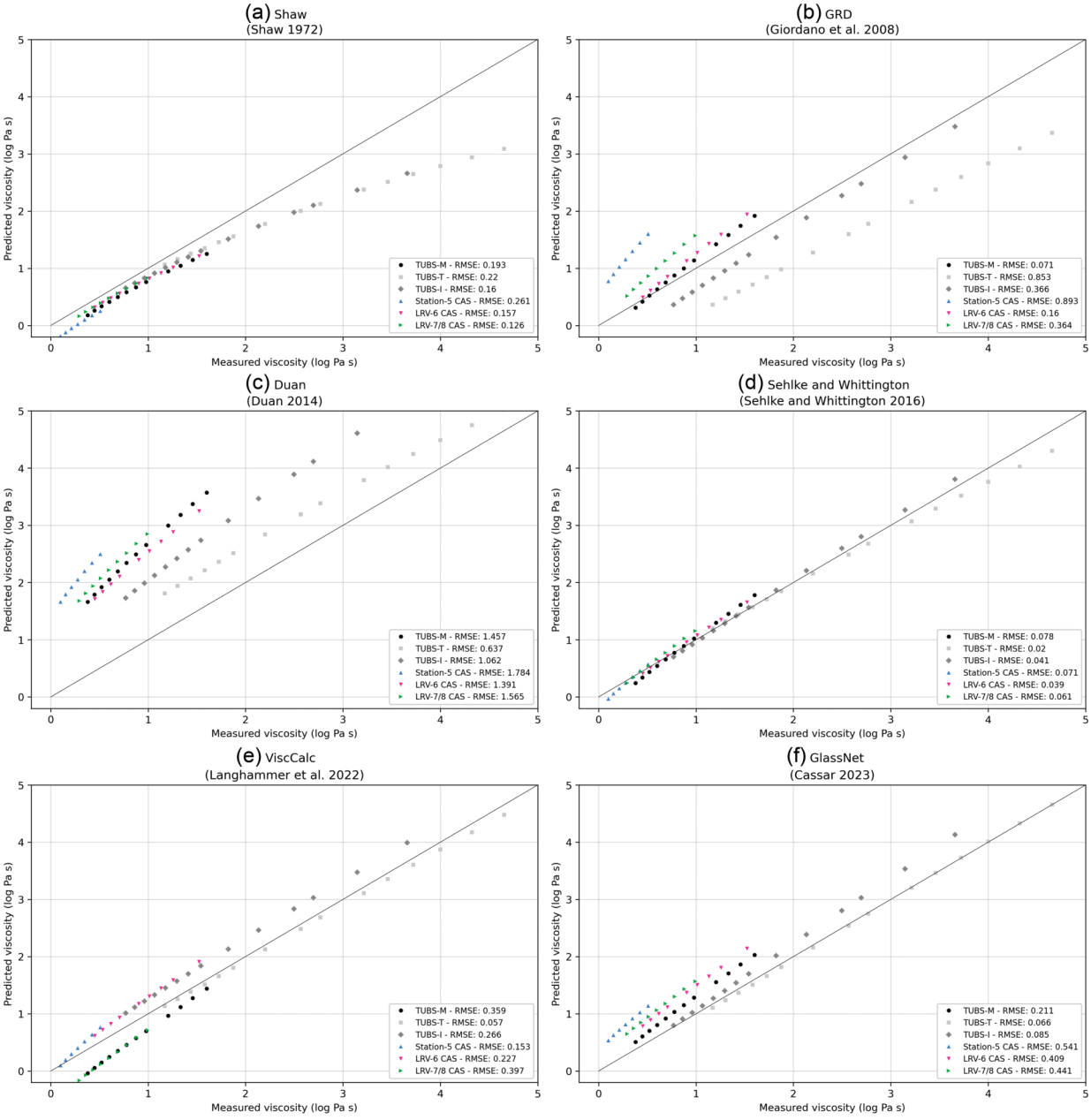

FIGURE 6. Comparison of measured viscosity data against predicted viscosities at high temperatures. All values given in log units.

ratio from 0.76 to 0.20 resulted in a remarkable increase in viscosity by approximately three orders of magnitude at a given temperature without altering the pattern of viscosity variation with temperature (Cukierman and Uhlmann 1974). These findings correlate well with research done by Chevrel et al. (2013), where viscosity and glass transition temperatures decrease for more-reduced melts until a threshold of $Fe^{2+}/Fe_{tot} = 0.5$ is reached. The calculated iron oxidation state of roughly 0.6 for all samples brings the studied melts close to the threshold ($Fe^{2+}/Fe_{tot} = 0.5$) at which the glass transition temperature no longer decreases with the redox state but remains constant (Chevrel et al. 2013).

Cooling behavior

To investigate the influence of fragility and viscosity on the 3D printing process with molten lunar regolith, the cooling behavior of the different melts in vacuum needs to be understood. The cooling process in vacuum is mainly governed by radiative heat transfer, described by the differential equation:

$$\frac{dT}{dt} = -\frac{\epsilon\sigma A}{mc}(T^4 - T_{env}^4)$$

where ϵ is the emissivity, σ is the Stefan-Boltzmann constant, A is the surface area, m is the mass, c is the specific heat capacity, T is the temperature of the object, and T_{env} is the ambient

temperature (here: 293.15 K). The melts to be used in the 3D printing process are expected to be at the working temperature (here: at 10^3 Pa s) and are defined to solidify at the temperature at the softening point ($10^{6.6}$ Pa s), which is where liquids stop to deform under their own weight. To get the cooling time of the melts by radiation, the differential equation is solved for time:

$$t_{\text{cooling}} = -\frac{mc}{\epsilon\sigma A}\int_{T(\eta=10^{3}\ \text{Pa s})}^{T(\eta=10^{6.6}\ \text{Pa s})}\frac{dT}{T^4 - T_{\text{env}}^4}$$

which can further be simplified by assuming that the variables are equal for each melt:

$$C = \int_{T(\eta=10^{3}\ \text{Pa s})}^{T(\eta=10^{6.6}\ \text{Pa s})}\frac{dT}{T^4 - T_{\text{env}}^4}$$

where C is a normalized "Cooling Value" that indicates the time that a melt needs to reach the softening point and, therefore, does not flow under its own weight. While the "Cooling Value" does not depend on the emissivity and heat capacity, it is important to note that the emissivity and heat capacity heavily influence the cooling behavior of the melt and, therefore, need to be considered if these properties are known. Due to the faster radiative cooling at higher temperatures, it is evident that melts with a high temperature at the working point have lower "Cooling Values," as they reach the softening point faster and are therefore more suitable for particular 3D printing applications where quick solidification is required. Based on the calculations, the highland TUBS-T simulant solidifies most quickly in a vacuum environment. The calculated "Cooling Values" for the tested simulants are displayed in Table 7.

Implications

When determining the optimal lunar regolith for 3D printing, several factors related to the melting and solidification behavior of the melts must be considered. For technological purposes, melts with a low melting point are preferred, as they generally require less energy to melt and get fluid enough to be worked. Operating at lower temperatures enables the usage of a wider diversity of materials for the hot zone of the furnace and reduces wear and tear, minimizing the need to repair after longer use. This argument favors the use of mare regolith over highland regolith from a technical point of view.

In terms of fragility, more fragile melts may be preferred as the viscosity changes faster in the high-temperature and working range regime, meaning that fragile melts reach the softening point faster and, therefore, freeze their shape faster than strong glasses, which is beneficial for extrusion-based 3D printing applications, rendering fragile melts more suitable in this regard. Stronger melts need a higher change of temperature to get from the melting point to the softening point and less temperature change to get from the softening point to the glass transition than fragile melts. Since most of the tested melts have fragility values within a similar range, the cooling rates of the melts are expected to have a greater influence on the solidification than the fragility. Melts that require higher temperatures to reach their working point can provide benefits in terms of cooling behavior. Since radiative heat transfer is proportional to the fourth power of the temperature, higher-temperature melts cool more rapidly, leading to a faster increase in viscosity. These properties are advantageous in processes that demand rapid solidification of the melt and where energy consumption is not a primary concern.

Table 7. Comparison of the "Cooling Value" of the different simulants between the liquidus temperature and the softening temperature, calculated by using the VFT parameters

Simulant name	Working temperature[a] in K (at $\eta = 10^3$ Pa s)	Softening temperature[a] in K (at $\eta = 10^{6.6}$ Pa s)	"Cooling Value"[b] in $1/T^4$
TUBS-M	1286	1067	118.72×10^{-12}
TUBS-T	1493	1234	77.44×10^{-12}
TUBS-I	1388	1125	109.14×10^{-12}
LRV-6 CAS	1362	1108	91.21×10^{-12}
LRV-7/8 CAS	1282	1085	103.31×10^{-12}

[a] Calculated using the VFT parameters.
[b] Calculated by $C = \int_{T(\eta=10^{3}\ \text{Pa s})}^{T(\eta=10^{6.6}\ \text{Pa s})}\frac{dT}{T^4 - T_{\text{env}}^4}$.

As shown by Cukierman and Uhlmann (1974), reduced melts have a lower glass transition temperature while maintaining the viscosity-temperature variation pattern. On the other hand, reduced melts have lower viscosities than oxidized melts (Cukierman and Uhlmann 1974; Dingwell and Virgo 1987; Liebske et al. 2003; Bouhifd et al. 2004; Chevrel et al. 2013, 2014; Di Genova et al. 2017), reducing the required energy to reach the working temperature. The lower glass transition temperature in reduced melts could also facilitate the annealing of 3D-printed structures, as cooling through radiation at decreased temperatures is reduced, keeping the glass in the annealing range for a longer period. This indicates that reduced melts, which would be created on the Moon, may even be more suitable for extrusion-based, 3D printing processes with molten lunar regolith than the highly oxidized Earth-found materials.

The significant variability in the viscosities of lunar regolith simulants is a key factor in site selection, especially when using processes that utilize molten lunar regolith. On one hand, the lower viscosities expected of regolith in the lunar mare areas will produce melts that require lower temperatures to achieve the desired viscosity compared to the regolith of the lunar highlands. On the other hand, highland regolith requires higher temperatures to reach the desired viscosity, which results in faster cooling to the softening point, allowing it to retain its shape more quickly. The choice of feedstock material will depend on the application, as different conditions and requirements may favor different material properties. For extrusion-based processes, the authors recommend using a mare regolith simulant due to its lower temperature requirements and higher fragility. Highland regolith simulants are not generally worse, as their advantage of faster cooling to the softening point, as indicated by a low "Cooling Value" value, may offer a major advantage over mare simulants. Since the cooling behavior and crystallization of the melt are decisive for the material properties of the solidified bodies, these aspects should be investigated in more detail in future work. Given the planned Artemis Base Camp at the lunar south pole (Creech et al. 2022), the highland regolith present in that region appears to be a well-suited option for additive manufacturing using molten lunar regolith, assuming that the higher energy requirements can be managed.

The influence of heavily reduced regolith melts on the Moon requires further investigation. The reduction in viscosity could

be advantageous not only for energy efficiency but also for allowing the use of lower-cost materials in the furnace, such as heaters, crucibles, and insulation, due to the reduced temperature requirements. Additionally, the resulting lower glass transition temperature of reduced melts may aid in the annealing of the molten regolith. However, it also increases the cooling time to the softening point, where the melt no longer deforms under its own weight.

The model by Sehlke and Whittington (2016) is recommended for predicting the high-temperature viscosity of lunar regolith in additive manufacturing applications. The study revealed that current models fail to accurately predict viscosities at the glass transition temperature, underscoring the necessity for additional research in this domain.

Acknowledgments and Funding

This work and the corresponding author are funded by the DLR Space Administration with funds provided by the Federal Ministry for Economic Affairs and Climate Action (BMWK) under grant numbers 50WM2057 (Project EDAM-R) and 50WM2445 (Project 3D-LAVA). D.B.D. acknowledges the support of ERC 2018 ADV Grant no. 834225 (EAVESDROP). J.S. acknowledges funding from the European Union's Horizon 2020 research and innovation program under the Marie Skłodowska-Curie grant agreement No. 847439. The corresponding author would like to express his gratitude to K'a-dag Gautama Lamleh for being a constant source of inspiration and for providing a calming presence during the writing process of this manuscript.

References Cited

Angell, C. (1991) Relaxation in liquids, polymers and plastic crystals—Strong/fragile patterns and problems. Journal of Non-Crystalline Solids 131-133, 13–31, https://doi.org/10.1016/0022-3093(91)90266-9.

Avramov, I. (2011) Dependence of the parameters of equations of viscous flow on chemical composition of silicate melts. Journal of Non-Crystalline Solids 357, 3841–3846, https://doi.org/10.1016/j.jnoncrysol.2011.07.031.

Böhmer, R. and Angell, C.A. (1992) Correlations of the nonexponentiality and state dependence of mechanical relaxations with bond connectivity in Ge-As-Se supercooled liquids. Physical Review B: Condensed Matter 45, 10091–10094, https://doi.org/10.1103/PhysRevB.45.10091.

Bottinga, Y. and Weill, D. (1972) The viscosity of magmatic silicate liquids; a model calculation. American Journal of Science 272, 438–475, https://doi.org/10.2475/ajs.272.5.438.

Bouhifd, M., Richet, P., Besson, P., Roskosz, M., and Ingrin, J. (2004) Redox state, microstructure and viscosity of a partially crystallized basalt melt. Earth and Planetary Science Letters 218, 31–44, https://doi.org/10.1016/S0012-821X(03)00641-1.

Cassar, D.R. (2023) GlassNet: A multitask deep neural network for predicting many glass properties. Ceramics International 49, 36013–36024, https://doi.org/10.1016/j.ceramint.2023.08.281.

Cesaretti, G., Dini, E., de Kestelier, X., Colla, V., and Pambaguian, L. (2014) Building components for an outpost on the Lunar soil by means of a novel 3D printing technology. Acta Astronautica 93, 430–450, https://doi.org/10.1016/j.actaastro.2013.07.034.

Chevrel, M.O., Giordano, D., Potuzak, M., Courtial, P., and Dingwell, D.B. (2013) Physical properties of $CaAl_2Si_2O_8$-$CaMgSi_2O_6$-FeO-Fe_2O_3 melts: Analogues for extra-terrestrial basalt. Chemical Geology 346, 93–105, https://doi.org/10.1016/j.chemgeo.2012.09.004.

Chevrel, M.O., Baratoux, D., Hess, K.-U., and Dingwell, D.B. (2014) Viscous flow behavior of tholeiitic and alkaline Fe-rich martian basalts. Geochimica et Cosmochimica Acta 124, 348–365, https://doi.org/10.1016/j.gca.2013.08.026.

Crawford, I.A. (2004) The scientific case for renewed human activities on the Moon. Space Policy 20, 91–97, https://doi.org/10.1016/j.spacepol.2004.02.007.

Creech, S., Guidi, J., and Elburn, D. (2022) Artemis: An Overview of NASA's Activities to Return Humans to the Moon, 2022 IEEE Aerospace Conference (AERO). IEEE.

Cukierman, M. and Uhlmann, D.R. (1974) Effects of iron oxidation state on viscosity, lunar composition 15555. Journal of Geophysical Research: Solid Earth 79, 1594–1598, https://doi.org/10.1029/JB079i011p01594.

Di Genova, D., Romano, C., Hess, K.-U., Vona, A., Poe, B.T., Giordano, D., Dingwell, D.B., and Behrens, H. (2013) The rheology of peralkaline rhyolites from Pantelleria Island. Journal of Volcanology and Geothermal Research 249, 201–216, https://doi.org/10.1016/j.jvolgeores.2012.10.017.

Di Genova, D., Vasseur, J., Hess, K.-U., Neuville, D.R., and Dingwell, D.B. (2017) Effect of oxygen fugacity on the glass transition, viscosity and structure of silica- and iron-rich magmatic melts. Journal of Non-Crystalline Solids 470, 78–85, https://doi.org/10.1016/j.jnoncrysol.2017.05.013.

Dingwell, D.B. (1986) Viscosity-temperature relationships in the system $Na_2Si_2O_5$-$Na_4Al_2O_5$. Geochimica et Cosmochimica Acta 50, 1261–1265, https://doi.org/10.1016/0016-7037(86)90409-6.

——— (1989) Shear viscosities of ferrosilicate liquids. American Mineralogist 74, 1038–1044.

——— (1991) Redox viscometry of some Fe-bearing silicate melts. American Mineralogist 76, 1560–1562.

——— (2006) Transport properties of magmas: Diffusion and rheology. Elements 2, 281–286, https://doi.org/10.2113/gselements.2.5.281.

Dingwell, D.B. and Virgo, D. (1987) The effect of oxidation state on the viscosity of melts in the system Na_2O-FeO-Fe_2O_3-SiO_2. Geochimica et Cosmochimica Acta 51, 195–205, https://doi.org/10.1016/0016-7037(87)90231-6.

——— (1988) Viscosities of melts in the Na_2O-FeO-Fe_2O_3-SiO_2 system and factors controlling relative viscosities of fully polymerized silicate melts. Geochimica et Cosmochimica Acta 52, 395–403, https://doi.org/10.1016/0016-7037(88)90095-6.

Dingwell, D.B. and Webb, S.L. (1989) Structural relaxation in silicate melts and non-Newtonian melt rheology in geologic processes. Physics and Chemistry of Minerals 16, 508–516, https://doi.org/10.1007/BF00197020.

Dingwell, D.B., Brearley, M., and Dickinson, J.E. Jr. (1988) Melt densities in the Na_2O-FeO-Fe_2O_3-SiO_2 system and the partial molar volume of tetrahedrally-coordinated ferric iron in silicate melts. Geochimica et Cosmochimica Acta 52, 2467–2475, https://doi.org/10.1016/0016-7037(88)90305-5.

Dingwell, D.B., Hess, K.-U., Wilding, M.C., Brooker, R.A., Di Genova, D., Drewitt, J.W., Wilson, M., and Weidendorfer, D. (2022) The glass transition and the non-Arrhenian viscosity of carbonate melts. American Mineralogist 107, 1053–1064, https://doi.org/10.2138/am-2021-7752.

Duan, X. (2014) A model for calculating the viscosity of natural iron-bearing silicate melts over a wide range of temperatures, pressures, oxygen fugacites, and compositions. American Mineralogist 99, 2378–2388, https://doi.org/10.2138/am-2014-4841.

Dunlop, D.J. (1973) Superparamagnetic and single-domain threshold sizes in magnetite. Journal of Geophysical Research: Solid Earth 78, 1780–1793, https://doi.org/10.1029/JB078i011p01780.

Dunlop, D.J. and Özdemir, Ö. (1997) Rock Magnetism: Fundamentals and Frontiers, 573 p. Cambridge University Press.

Fabes, B.D. and Poisl, W.H. (1991) Processing of glass-ceramics from lunar resources, # 19910015067. NASA Space Engineering Research Center for Utilization of Local Planetary Resources.

Farries, K.W., Visintin, P., Smith, S.T., and van Eyk, P. (2021) Sintered or melted regolith for lunar construction: State-of-the-art review and future research directions. Construction & Building Materials 296, 123627, https://doi.org/10.1016/j.conbuildmat.2021.123627.

Fateri, M., Pitikaris, S., and Sperl, M. (2019a) Investigation on wetting and melting behavior of lunar regolith simulant for additive manufacturing application. Microgravity Science and Technology 31, 161–167, https://doi.org/10.1007/s12217-019-9674-5.

Fateri, M., Meurisse, A., Sperl, M., Urbina, D., Madakashira, H.K., Govindaraj, S., Gancet, J., Imhof, B., Hoheneder, W., Waclavicek, R., and others. (2019b) Solar sintering for lunar additive manufacturing. Journal of Aerospace Engineering 32, 04019101, https://doi.org/10.1061/(ASCE)AS.1943-5525.0001093.

Fulcher, G.S. (1925) Analysis of recent measurements of the viscosity of glasses. Journal of the American Ceramic Society 8, 339–355, https://doi.org/10.1111/j.1151-2916.1925.tb16731.x.

Gerdes, N., Fokken, L.G., Linke, S., Kaierle, S., Suttmann, O., Hermsdorf, J., Stoll, E., and Trentlage, C. (2018) Selective Laser Melting for processing of regolith in support of a lunar base. Journal of Laser Applications 30, 032018, https://doi.org/10.2351/1.5018576.

Ginés-Palomares, J.-C., Fateri, M., Schubert, T., de Peindray d'Ambelle, L., Simon, S., Gluth, G.J.G., Günster, J., and Zocca, A. (2023a) Material aspects of sintering of EAC-1A lunar regolith simulant. Scientific Reports 13, 23053, https://doi.org/10.1038/s41598-023-50391-y.

Ginés-Palomares, J.-C., Fateri, M., Kalhöfer, E., Schubert, T., Meyer, L., Kolsch, N., Brandić Lipińska, M., Davenport, R., Imhof, B., Waclavicek, R., and others. (2023b) Laser melting manufacturing of large elements of lunar regolith simulant for paving on the Moon. Scientific Reports 13, 15593, https://doi.org/10.1038/s41598-023-42008-1.

Giordano, D. and Dingwell, D.B. (2003) Non-Arrhenian multicomponent melt viscosity: A model. Earth and Planetary Science Letters 208, 337–349, https://doi.org/10.1016/S0012-821X(03)00042-6.

Giordano, D., Russell, J.K., and Dingwell, D.B. (2008) Viscosity of magmatic liquids: A model. Earth and Planetary Science Letters 271, 123–134, https://doi.org/10.1016/j.epsl.2008.03.038.

Giordano, D., Ardia, P., Romano, C., Dingwell, D.B., Di Muro, A., Schmidt, M.W., Mangiacapra, A., and Hess, K.-U. (2009) The rheological evolution of alkaline Vesuvius magmas and comparison with alkaline series from the Phlegrean Fields, Etna, Stromboli and Teide. Geochimica et Cosmochimica Acta 73, 6613–6630, https://doi.org/10.1016/j.gca.2009.07.033.

Giuli, G., Paris, E., Pratesi, G., Koeberl, C., and Cipriani, C. (2003) Iron oxidation state in the Fe-rich layer and silica matrix of Libyan Desert Glass: A high-resolution XANES study. Meteoritics & Planetary Science 38, 1181–1186, https://doi.org/10.1111/j.1945-5100.2003.tb00306.x.

Giuli, G., Paris, E., Hess, K.-U., Dingwell, D.B., Cicconi, M.R., Eeckhout, S.G., Fehr, K.T., and Valenti, P. (2011) XAS determination of the Fe local environment and oxidation state in phonolite glasses. American Mineralogist 96, 631–636, https://doi.org/10.2138/am.2011.3464.

Gottsmann, J., Giordano, D., and Dingwell, D.B. (2002) Predicting shear viscosity during volcanic processes at the glass transition: A calorimetric calibration. Earth and Planetary Science Letters 198, 417–427, https://doi.org/10.1016/S0012-821X(02)00522-8.

Hess, K.U., Dingwell, D.B., and Webb, S.L. (1995) The influence of excess alkalis on the viscosity of a haplogranitic melt. American Mineralogist 80, 297–304, https://doi.org/10.2138/am-1995-3-411.

Hess, K.-U., Dingwell, D.B., and Rössler, E. (1996) Parametrization of viscosity-temperature relations of aluminosilicate melts. Chemical Geology 128, 155–163, https://doi.org/10.1016/0009-2541(95)00170-0.

Hufenbach, B., Reiter, T., and Sourgens, E. (2014) ESA strategic planning for space exploration. Space Policy 30, 174–177, https://doi.org/10.1016/j.spacepol.2014.07.009.

Jackson, W.E., de Leon, J.M., Brown, G.E. Jr., Waychunas, G.A., Conradson, S.D., and Combes, J.M. (1993) High-temperature XAS study of Fe_2SiO_4 liquid: Reduced coordination of ferrous iron. Science 262, 229–233, https://doi.org/10.1126/science.262.5131.229.

Johnson, S.W. and Chua, K.M. (1993) Properties and mechanics of the lunar regolith. Applied Mechanics Reviews 46, 285–300, https://doi.org/10.1115/1.3120358.

Kelton, K.F. (2017) Kinetic and structural fragility—A correlation between structures and dynamics in metallic liquids and glasses. Journal of Physics: Condensed Matter 29, 23002.

Kim, Y.-J., Ryu, B.H., Jin, H., Lee, J., and Shin, H.-S. (2021) Microstructural, mechanical, and thermal properties of microwave-sintered KLS-1 lunar regolith simulant. Ceramics International 47, 26891–26897, https://doi.org/10.1016/j.ceramint.2021.06.098.

Knipping, J.L., Behrens, H., Wilke, M., Göttlicher, J., and Stabile, P. (2015) Effect of oxygen fugacity on the coordination and oxidation state of iron in alkali bearing silicate melts. Chemical Geology 411, 143–154, https://doi.org/10.1016/j.chemgeo.2015.07.004.

Kress, V.C. and Carmichael, I.S.E. (1991) The compressibility of silicate liquids containing Fe_2O_3 and the effect of composition, temperature, oxygen fugacity and pressure on their redox states. Contributions to Mineralogy and Petrology 108, 82–92, https://doi.org/10.1007/BF00307328.

Lange, R.A. and Carmichael, I.S. (1987) Densities of Na_2O-K_2O-CaO-MgO-FeO-Fe_2O_3-Al_2O_3-TiO_2-SiO_2 liquids: New measurements and derived partial molar properties. Geochimica et Cosmochimica Acta 51, 2931–2946, https://doi.org/10.1016/0016-7037(87)90368-1.

Lange, R.A. and Carmichael, I.S.E. (1990) Thermodynamic properties of silicate liquids with emphasis on density, thermal expansion and compressibility. Reviews in Mineralogy and Geochemistry 24, 25–64.

Langhammer, D., Di Genova, D., and Steinle Neumann, G. (2022) Modeling viscosity of volcanic melts with artificial neural networks. Geochemistry, Geophysics, Geosystems 23, e2022GC010673, https://doi.org/10.1029/2022GC010673.

Lavallée, Y., Hess, K.-U., Cordonnier, B., and Bruce Dingwell, D. (2007) Non-Newtonian rheological law for highly crystalline dome lavas. Geology 35, 843, https://doi.org/10.1130/G23594A.1.

Le Bourhis, E. (2007) Glass: Mechanics and Technology, 390 p. Wiley.

Liebske, C., Behrens, H., Holtz, F., and Lange, R.A. (2003) The influence of pressure and composition on the viscosity of andesitic melts. Geochimica et Cosmochimica Acta 67, 473–485, https://doi.org/10.1016/S0016-7037(02)01139-0.

Linke, S. (2022) Mechanical material properties of laser-melted lunar regolith. Ph.D. thesis, Technische Universität Braunschweig (in German).

Linke, S., Windisch, L., Küter, N., Voß, A., Prizwara, P., Stoll, E., Schilde, C., and Kwade, A. (2018) TUBS-M and TUBS-T – New lunar regolith simulants adaptable to local surface characteristics. 69th International Astronautical Congress (IAC), Bremen, Germany.

Linke, S., Windisch, L., Kueter, N., Wanvik, J.E., Voss, A., Stoll, E., Schilde, C., and Kwade, A. (2020) TUBS-M and TUBS-T based modular Regolith Simulant System for the support of lunar ISRU activities. Planetary and Space Science 180, 104747, https://doi.org/10.1016/j.pss.2019.104747.

Linke, S., Voß, A., Ernst, M., Taschner, P.A., Baasch, J., Stapperfend, S., Gerdes, N., Koch, J., Weßels, P., Neumann, J., Overmeyer, L., and Stoll, E. (2022) Two-dimensional laser melting of lunar regolith simulant using the MOONRISE payload on a mobile manipulator. 3D Printing and Additive Manufacturing 9, 223–231, https://doi.org/10.1089/3dp.2020.0323.

Lucey, P., Korotev, R.L., Gillis, J.J., Taylor, L.A., Lawrence, D., Campbell, B.A., Elphic, R., Feldman, B., Hood, L.L., Hunten, D., and others. (2018) Understanding the lunar surface and space-Moon interactions. New Views of the Moon, 83–220.

Mackenzie, J. and Claridge, R. (1979) Glass and ceramics from lunar materials. 4th Conference on Space Manufacturing Facilities Princeton University, 14 May 1979–17 May 1979, Princeton, New Jersey, U.S.A. https://doi.org/10.2514/6.1979-1381.

Magnien, V., Neuville, D.R., Cormier, L., Roux, J., Hazemann, J.-L., de Ligny, D., Pascarelli, S., Vickridge, I., Pinet, O., and Richet, P. (2008) Kinetics and mechanisms of iron redox reactions in silicate melts: The effects of temperature and alkali cations. Geochimica et Cosmochimica Acta 72, 2157–2168, https://doi.org/10.1016/j.gca.2008.02.007.

Magoffin, M. and Garvey, J. (1990) Lunar glass production using concentrated solar energy. Space Programs and Technologies Conference, 25 September 1990–27 September 1990, Huntsville, Alabama, U.S.A. https://doi.org/10.2514/6.1990-3752.

Mauro, J.C., Yue, Y., Ellison, A.J., Gupta, P.K., and Allan, D.C. (2009) Viscosity of glass-forming liquids. Proceedings of the National Academy of Sciences of the United States of America, 106, 19780–19784, https://doi.org/10.1073/pnas.0911705106.

Meerlender, G. (1974) Viscosity temperature relation of the standard glass I of the Deutsche Glastechnische Gesellschaft (DGG). Glastechnische Berichte, 47, 1–3 (in German).

Meurisse, A., Makaya, A., Willsch, C., and Sperl, M. (2018) Solar 3D printing of lunar regolith. Acta Astronautica 152, 800–810, https://doi.org/10.1016/j.actaastro.2018.06.063.

Moretti, R. (2005) Polymerisation, basicity, oxidation state and their role in ionic modelling of silicate melts. Annals of Geophysics 48, 583–608.

Morrison, A.A., Zanetti, M., Hamilton, C.W., Lev, E., Neish, C.D., and Whittington, A.G. (2019) Rheological investigation of lunar highland and mare impact melt simulants. Icarus 317, 307–323, https://doi.org/10.1016/j.icarus.2018.08.001.

Mysen, B.O. (1988) Structure and Properties of Silicate Melts, 368 p. Elsevier.

Mysen, B.O., Virgo, D., and Seifert, F.A. (1984) Redox equilibria of iron in alkaline earth silicate melts: Relationships between melt structure, oxygen fugacity, temperature and properties of iron-bearing silicate liquids. American Mineralogist 69, 834–847.

Neuville, D.R. (2006) Viscosity, structure and mixing in (Ca, Na) silicate melts. Chemical Geology 229, 28–41, https://doi.org/10.1016/j.chemgeo.2006.01.008.

Persikov, E.S., Zharikov, V.A., and Bukhtiyarov, P.G. (1990) The effect of volatiles on the properties of magmatic melts. European Journal of Mineralogy 2, 621–642, https://doi.org/10.1127/ejm/2/5/0621.

Plazek, D.J. and Ngai, K.L. (1991) Correlation of polymer segmental chain dynamics with temperature-dependent time-scale shifts. Macromolecules 24, 1222–1224, https://doi.org/10.1021/ma00005a044.

Ray, C.S., Reis, S.T., Sen, S., and O'Dell, J.S. (2010) JSC-1A lunar soil simulant: Characterization, glass formation, and selected glass properties. Journal of Non-Crystalline Solids 356, 2369–2374, https://doi.org/10.1016/j.jnoncrysol.2010.04.049.

Reitz, B., Lotz, C., Gerdes, N., Linke, S., Olsen, E., Pflieger, K., Sohrt, S., Ernst, M., Taschner, P., Neumann, J., and others. (2021) Additive manufacturing under lunar gravity and microgravity. Microgravity Science and Technology 33, 25, https://doi.org/10.1007/s12217-021-09878-4.

Richet, P. (1984) Viscosity and configurational entropy of silicate melts. Geochimica et Cosmochimica Acta 48, 471–483, https://doi.org/10.1016/0016-7037(84)90275-8.

Richet, P. and Bottinga, Y. (1986) Thermochemical properties of silicate glasses and liquids: A review. Reviews of Geophysics 24, 1–25, https://doi.org/10.1029/RG024i001p00001.

Romano, C., Giordano, D., Papale, P., Mincione, V., Dingwell, D.B., and Rosi, M. (2003) The dry and hydrous viscosities of alkaline melts from Vesuvius and Phlegrean Fields. Chemical Geology 202, 23–38, https://doi.org/10.1016/S0009-2541(03)00208-0.

Russell, J.K., Hess, K.-U., and Dingwell, D.B. (2022) Models for viscosity of geological melts. Reviews in Mineralogy and Geochemistry 87, 841–885, https://doi.org/10.2138/rmg.2022.87.18.

Schleppi, J., Gibbons, J., Groetsch, A., Buckman, J., Cowley, A., and Bennett, N. (2019) Manufacture of glass and mirrors from lunar regolith simulant. Journal of Materials Science 54, 3726–3747, https://doi.org/10.1007/s10853-018-3101-y.

Schleppi, J., Bromiley, G., Odling, N., and Bennett, N.S. (2021) In-situ resource utilisation manufacturing of optically transparent glass from lunar regolith simulant. Journal of Materials Science 56, 12132–12153, https://doi.org/10.1007/s10853-021-06059-x.

Sehlke, A. and Whittington, A.G. (2016) The viscosity of planetary tholeiitic melts: A configurational entropy model. Geochimica et Cosmochimica Acta 191, 277–299, https://doi.org/10.1016/j.gca.2016.07.027.

——— (2020) Rheology of a KREEP analog magma: Experimental results applied to dike ascent through the lunar crust. Planetary and Space Science 187, 104941, https://doi.org/10.1016/j.pss.2020.104941.

Sehlke, A., Whittington, A., Robert, B., Harris, A., Gurioli, L., and Médard, E. (2014) Pahoehoe to 'a'a transition of Hawaiian lavas: An experimental study. Bulletin of Volcanology 76, 876, https://doi.org/10.1007/s00445-014-0876-9.

Shaw, H.R. (1972) Viscosities of magmatic silicate liquids; an empirical method of prediction. American Journal of Science 272, 870–893, https://doi.org/10.2475/ajs.272.9.870.

Stabile, P., Webb, S., Knipping, J.L., Behrens, H., Paris, E., and Giuli, G. (2016) Viscosity of pantelleritic and alkali-silicate melts: Effect of Fe redox state and

Na/(Na + K) ratio. Chemical Geology 442, 73–82, https://doi.org/10.1016/j.chemgeo.2016.09.003.
Stapperfend, S., Linke, S., Hess, K.-U., Dingwell, D.B., and Stoll, E. (2023) Additive manufacturing with molten lunar regolith under vacuum conditions. 74th International Astronautical Congress, Baku, Azerbaijan.
Street, J.W., Ray, C., Rickman, D., and Scheiman, D.A. (2010) Thermal properties of lunar regolith simulants. In G. Song and R.B. Malla, Eds., Earth and Space 2010: Engineering, Science, Construction, and Operations in Challenging Environments, p. 266–275, ASCE.
Sutherland, J., Mueller, A., Dingwell, D.B., Stoll, E., Stapperfend, S., and Hansen, T. (2022) High-temperature characterisation of improved fidelity lunar regolith simulants, Abstract G0.4-0002-22. 44th COSPAR Scientific Assembly, 16–24 July, 2022, https://www.cosparathens2022.org/.
Tammann, G. and Hesse, W. (1926) The dependence of viscosity upon the temperature of supercooled liquids. Zeitschrift für Anorganische und Allgemeine Chemie 156, 245–257, https://doi.org/10.1002/zaac.19261560121 (in German).
Taylor, L.A. and Meek, T.T. (2005) Microwave sintering of lunar soil: Properties, theory, and practice. Journal of Aerospace Engineering 18, 188–196, https://doi.org/10.1061/(ASCE)0893-1321(2005)18:3(188).
Toplis, M.J. and Carroll, M.R. (1995) An experimental study of the influence of oxygen fugacity on Fe-Ti oxide stability, phase relations, and mineral-melt equilibria in ferro-basaltic systems. Journal of Petrology 36, 1137–1170, https://doi.org/10.1093/petrology/36.5.1137.
Toplis, M.J., Dingwell, D.B., and Libourel, G. (1994) The effect of phosphorus on the iron redox ratio, viscosity, and density of an evolved ferro-basalt. Contributions to Mineralogy and Petrology 117, 293–304, https://doi.org/10.1007/BF00310870.
Toplis, M.J., Dingwell, D.B., Hess, K.-U., and Lenci, T. (1997) Viscosity, fragility, and configurational entropy of melts along the join SiO_2-$NaAlSiO_4$. American Mineralogist 82, 979–990, https://doi.org/10.2138/am-1997-9-1014.
Villeneuve, N., Neuville, D.R., Boivin, P., Bachèlery, P., and Richet, P. (2008) Magma crystallization and viscosity: A study of molten basalts from the Piton de la Fournaise volcano (La Réunion island). Chemical Geology 256, 242–251, https://doi.org/10.1016/j.chemgeo.2008.06.039.
Vogel, H. (1921) The law of the relation between the viscosity of liquids and the temperature. Physikalische Zeitschrift, 22, 645–646 (in German).
Webb, S.L. and Dingwell, D.B. (1990) The onset of non-Newtonian rheology of silicate melts. Physics and Chemistry of Minerals 17, 125–132, https://doi.org/10.1007/BF00199663.
Whittington, A. and Parsapoor, A. (2022) Lower cost lunar bricks: Energetics of melting and sintering lunar regolith simulants. New Space 10, 193–204, https://doi.org/10.1089/space.2021.0055.
Wieczorek, M.A. (2006) The constitution and structure of the lunar interior. Reviews in Mineralogy and Geochemistry 60, 221–364, https://doi.org/10.2138/rmg.2006.60.3.
Wilhelm, S. and Curbach, M. (2014) Review of possible mineral materials and production techniques for a building material on the moon. Structural Concrete 15, 419–428, https://doi.org/10.1002/suco.201300088.
Wilke, M., Farges, F., Petit, P.-E., Brown, G.E. Jr., Martin, F. (2001) Oxidation state and coordination of Fe in minerals: An Fe K- XANES spectroscopic study. American Mineralogist 86, 714–730, https://doi.org/10.2138/am-2001-5-612.
Wilke, M., Schmidt, C., Farges, F., Malavergne, V., Gautron, L., Simionovici, A., Hahn, M., and Petit, P.-E. (2006) Structural environment of iron in hydrous aluminosilicate glass and melt-evidence from X-ray absorption spectroscopy. Chemical Geology 229, 144–161, https://doi.org/10.1016/j.chemgeo.2006.01.017.
Zheng, Q. and Mauro, J.C. (2017) Viscosity of glass forming systems. Journal of the American Ceramic Society 100, 6–25, https://doi.org/10.1111/jace.14678.
Zocca, A., Fateri, M., Al-Sabbagh, D., and Günster, J. (2020) Investigation of the sintering and melting of JSC-2A lunar regolith simulant. Ceramics International 46, 14097–14104, https://doi.org/10.1016/j.ceramint.2020.02.212.

Manuscript received November 27, 2023
Manuscript accepted October 25, 2024
Accepted manuscript online November 5, 2024
Manuscript Handled by Zhicheng Jing